Discerning element and site-specific fluctuations of the charge-orbital order in Fe_3O_4 below the Verwey transition

Nelson Hua,[1,2] Jianheng Li,[3] Stjepan B. Hrkac,[1] Andi Barbour,[4] Wen Hu,[4] Claudio Mazzoli,[4] Stuart Wilkins,[4] Roopali Kukreja,[3,*] Eric E. Fullerton,[1,2] and Oleg G. Shpyrko[1,2,*]

[1]*Department of Physics, University of California, San Diego, La Jolla, California 92093, USA*

[2]*Center for Memory and Recording Research, University of California, San Diego, La Jolla, California 92093, USA*

[3]*Department of Materials Science Engineering, University of California-Davis, Davis, California 95616, USA*

[4]*National Synchrotron Light Source II, Brookhaven National Laboratory, Upton, New York 11973, USA*

(Received 14 April 2020; revised 16 November 2022; accepted 6 January 2023; published 31 January 2023)

Despite countless experimental probes into magnetite's electronic structure across the Verwey transition Fe_3O_4, the exact origin of this archetypical metal-insulator transition remains a puzzle. Advanced x-ray diffraction techniques have mostly resolved the monoclinic structure of the insulating phase, including interatomic bond lengths, but the complexity of the charge-orbitally ordered state is difficult to disentangle. We combined resonant elastic x-ray scattering and x-ray photon correlation spectroscopy to probe charge-orbital fluctuations in the insulating state of magnetite. By accessing the Bragg forbidden $(00\frac{1}{2})_c$ peak at the oxygen K-edge, we complement our previous study on the iron L_3-edge to reveal the dynamics of the iron $3d$ and oxygen $2p$ orbital domains. Our new results reveal a decoupling of the orbital correlation lengths between the oxygen $2p$ states and site-specific iron $3d$ states, and we further show charge-orbital domain fluctuations at the iron t_{2g} orbital sites of trimeron chains. These results also demonstrate an experimental method capable of distinguishing electronic dynamics between the oxygen ligands and the transition metal that underpins emergent behaviors in complex oxides.

DOI: 10.1103/PhysRevMaterials.7.014413

I. INTRODUCTION

Macroscopic phenomena in transition-metal oxides such as superconductivity, colossal magnetoresistance, and metal-insulator transitions are manifestations of the correlations between the electronic and lattice structures at the atomic scale [1–3]. Resolving competing order parameters originating from the electron spin, charge, and orbital states as well as mesoscale effects such as domain wall evolution is key to understanding how to tailor these materials for electronic applications. One approach to resolving various structural and electronic order parameters is with elastic x-ray scattering techniques, which have been frequently used to study the role of the transition metal [4–7]. However, the role of the oxygen ligands is often neglected given that the accessibility of oxygen in scattering is often difficult or impossible to reach, and many techniques such as x-ray magnetic circular and linear dichroism only make sense about the transition metal resonant edges. In this study, we use a coherent x-ray scattering technique known as x-ray photon correlation spectroscopy (XPCS) at the oxygen K-edge resonance to study possible dynamic behavior of oxygen in Fe_3O_4 that would otherwise be hidden from standard x-ray diffraction techniques.

In magnetite (Fe_3O_4), the mechanism behind its metal-insulator transition, famously known as the Verwey transition, continues to confound physicists. In the high-temperature metallic state, magnetite has a cubic inverse spinel structure consisting of two sublattices. The A sites are characterized by O^{2-} and Fe^{3+} ions that are tetrahedrally coordinated while B sites are octahedrally coordinated, consisting of O^{2-} ions and [Fe^{2+}, Fe^{3+}] ions in equal proportion [8,9]. The iron atoms of the A and B sites are also antiferromagnetically coupled through hybridization with the oxygen $2p$ orbitals. When magnetite is cooled below the transition temperature $T_V \sim 120$ K, a structural phase transition occurs where the cubic structure ($a = b = c = 8.387$ Å) distorts to a monoclinic one ($a = b = 11.88$ Å, $c = 16.775$ Å, and $\beta = 90.236°$) and is simultaneously accompanied by a drop in electrical conductivity by two to three orders of magnitude [10,11]. Verwey [11] postulated that this insulating state arises from the freezing of a B-site conduction electron into a charge-ordered state of alternating Fe^{2+} and Fe^{3+} on the octahedral sublattice. Although experiments have since disproven Verwey's original theory, a significantly more complex charge- and orbitally ordered insulating state is seen below the transition temperature.

In the monoclinic phase, cooperative Jahn-Teller (JT) distortions shorten interatomic bond lengths of B-site iron cations into linear three-site chains known as trimerons, the proposed order parameter describing the charge-orbitally ordered insulating state [12,13]. In particular, a trimeron consists of B-site iron atoms that are charge ordered in $Fe^{3+}-Fe^{2+}-Fe^{3+}$ chains, where the extra electron occupation of the degenerate iron t_{2g} orbitals gives rise to an additional orbitally ordered structure, as seen in Fig. 1(a). In

*rkukreja@ucdavis.edu and oshpyrko@ucsd.edu

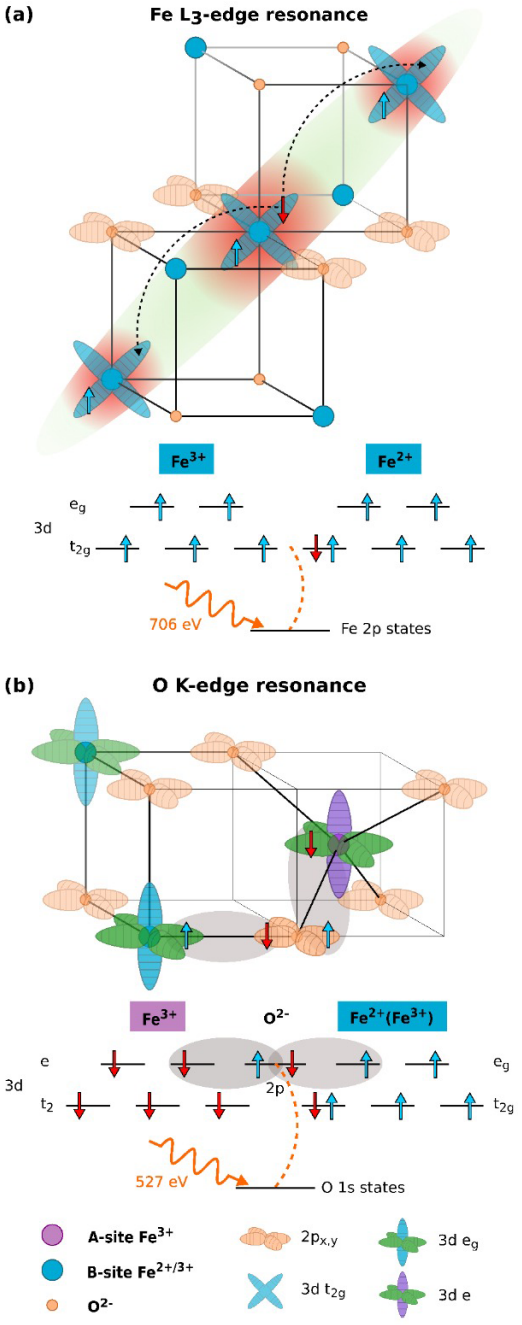

FIG. 1. (a) Iron L_3-edge resonance ($2p \rightarrow 3d$ states) probes the orbital occupancy of the t_{2g} electrons of, specifically, the B-site Fe^{2+} cations. Since the orbital order is not linked to lattice dynamics, the signal originates from delocalization of the minority spin electron within corner-sharing trimeron chains. The schematic shows one delocalization pathway where the extra electron in the central Fe^{2+} can hop directly to the neighboring Fe^{3+} t_{2g} sites along the trimeron. (b) The gray highlighted region shows examples of how the oxygen $2p$ orbitals are hybridized to the A and B iron sites, allowing for charge delocalization via superexchange and double-exchange interactions.

transition-metal oxides, Kugel and Khomskii have shown that orbital ordering arises from either JT coupling of electrons to the lattice or hopping of transition metal electrons into specific orbital states [14–16]. In the case of magnetite, the charge-orbital order manifests as a Bragg forbidden $(00\frac{1}{2})_c$ (the subscript denotes the cubic notation) peak that is accessible only at iron and oxygen resonant energies [17–19]. In other words, the charge-orbital anisotropy leads to a nonzero scattering factor at resonant energies [20]. The stability of this charge-orbital structure can be determined by changes in the orbital occupations at both the iron and oxygen sites [21]. Previously, we accessed the $(00\frac{1}{2})_c$ peak in scattering geometry at the iron L_3-edge to probe the iron $3d$ orbital occupancies via excitations from core to unoccupied valence states at the iron $2_{p3/2} \rightarrow 3d$ transitions [18]. The iron L_3-edge signal directly probes the B-site Fe^{2+} t_{2g} orbital structure, and our results showed dynamic orbital domain fluctuations in the low-temperature state. However, the results at the iron L_3-edge alone are not sufficient to pinpoint the origin of those fluctuations. We combined resonant elastic x-ray scattering and XPCS at the oxygen K-edge to investigate further the origin of these orbital fluctuations, whether it is due to structural domain reorientations or is purely electronic in nature. The resonant oxygen K-edge $(00\frac{1}{2})_c$ peak in scattering geometry directly probes the oxygen $2p$ orbital occupancies via excitations from core to unoccupied valence states at the oxygen $1s \rightarrow 2p$ transitions. Previous studies using resonant elastic x-ray scattering and local density approximation calculations show this peak arising from orbitally ordered oxygen $2p$ states. Since the oxygen $2p$ states are also hybridized to the iron $3d$ orbitals present on both the octahedral and tetrahedral sites, as seen in Figs. 1(a) and 1(b) [18,19,22–24], we can also indirectly probe the iron $3d$ state. Previous simulations have shown this signal to be mostly sensitive to the hybridization to the B-site Fe^{3+} ions. Our studies show a lack of electronic fluctuations at the oxygen K-edge, indicating an extremely stable oxygen $2p$ orbital network in the low-temperature monoclinic phase where there is an absence of ligand-to-metal charge transfer dynamics in equilibrium. This implies that the thermally active fluctuations previously observed in the iron t_{2g} orbital domains is due to the delocalization of the minority spin electron between adjacent B-site iron cations within trimeron chains, as postulated by Senn *et al.* [12]. Our XPCS studies at both the iron L_3-edge and the oxygen K-edge are now able to confirm this scenario experimentally.

II. EXPERIMENT AND RESULTS

The resonant XPCS experiment was conducted at the Coherent Soft X-ray beamline at the National Synchrotron Light Source II. A schematic of the experimental scattering geometry is shown in Fig. 2, where a coherent x-ray beam is tuned to the iron L_3-edge (705.7 eV) and oxygen K-edge (527.2 eV) resonant energies to probe the $(00\frac{1}{2})_c$ peak, where the slight offset from literature values is due to the calibration at the beamline. The resonant energy at the iron L_3-edge corresponds to the maximum scattered intensity at the $(00\frac{1}{2})_c$ Bragg condition, which was previously shown to be mainly due to the B-site Fe^{2+} cations from the decomposition of the x-ray absorption spectroscopy (XAS) spectrum [18,22,25]. The oxygen K-edge resonant energy was also optimized to the maximum scattering intensity at the $(00\frac{1}{2})_c$ Bragg condition corresponding to the pre-edge of the oxygen K-edge XAS

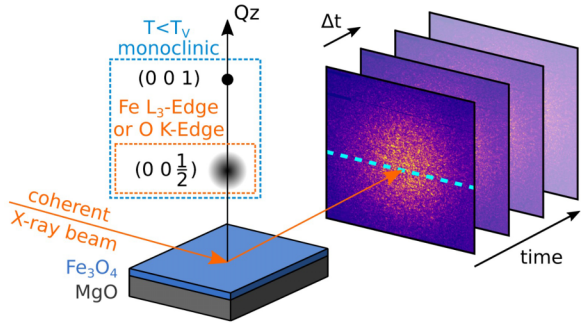

FIG. 2. Experimental setup of the XPCS experiment where coherent soft x-rays are tuned to the iron L_3-edge (705.7 eV) and the oxygen K-edge (527.2 eV) to access the $(00\frac{1}{2})_c$ peak that only exists in the low-temperature monoclinic phase at resonance. Shown is a CCD detector image of the $(00\frac{1}{2})_c$ peak at the oxygen K-edge resonant energy at 27 K. The (001) lattice peak is also a forbidden peak that can be accessed in the low-temperature state, though not necessarily at resonance. A CCD records the speckle pattern of the $(00\frac{1}{2})_c$ peak at the oxygen K-edge resonance with a delay time of Δt between each image.

profile [19]. The (001) lattice peak is also only accessible in the monoclinic phase based on the crystal symmetry of the low-temperature state [17]. Therefore, we also monitored the (001) lattice peak profile off resonance at 800 eV to follow the correlation length of the structural order independently. A charge-coupled device (CCD) detector with a 30-μm×30-μm pixel size located 34 cm from the sample was used to record the measurements, and an example of the detector image for the $(00\frac{1}{2})_c$ peak at the oxygen K-edge resonance is shown in Fig. 2. The degree of contrast can be visualized from a line cut through the central speckle pattern, as shown in Fig. 3(a). A Gaussian function was used to fit the peak where the full-width-at-half-maximum (FWHM) in reciprocal space, ΔQ, is used to define the correlation length $\lambda = 1/\Delta Q$. Superimposed in Fig. 3(a) is the (001) lattice peak at 800 eV, which shows the correlation length of the lattice structure is approximately 10 times greater than the charge-orbital correlation length, indicating the oxygen $2p$ orbital domains are not defined by structural domain boundaries. The $(00\frac{1}{2})_c$ peak at the oxygen K-edge resonance was measured between 25 K and 109 K, and its correlation length and integrated peak intensity as a function of temperature are shown in Fig. 3(b). The correlation lengths of the $(00\frac{1}{2})_c$ peak at the oxygen K-edge and iron L_3-edge well below the Verwey transition temperature are approximately 13 nm and 16 nm, respectively, which is consistent with literature data [18,26,27].

The speckle pattern overlaid on the $(00\frac{1}{2})_c$ peak is the fundamental attribute in the XPCS technique that allows us to measure dynamics of the system. When a coherent beam interacts with the nanoscale heterogeneities—in this, case charge-orbital domains—the interference between the coherent beam and the nanoscale heterogeneities creates the speckle pattern seen within the $(00\frac{1}{2})_c$ peak. Since we have a stable coherent beam, any fluctuations of the charge-orbital domains manifest as spatial and temporal intensity changes in the speckle pattern. Therefore, by correlating the intensity of successive speckle patterns, it is possible to resolve the

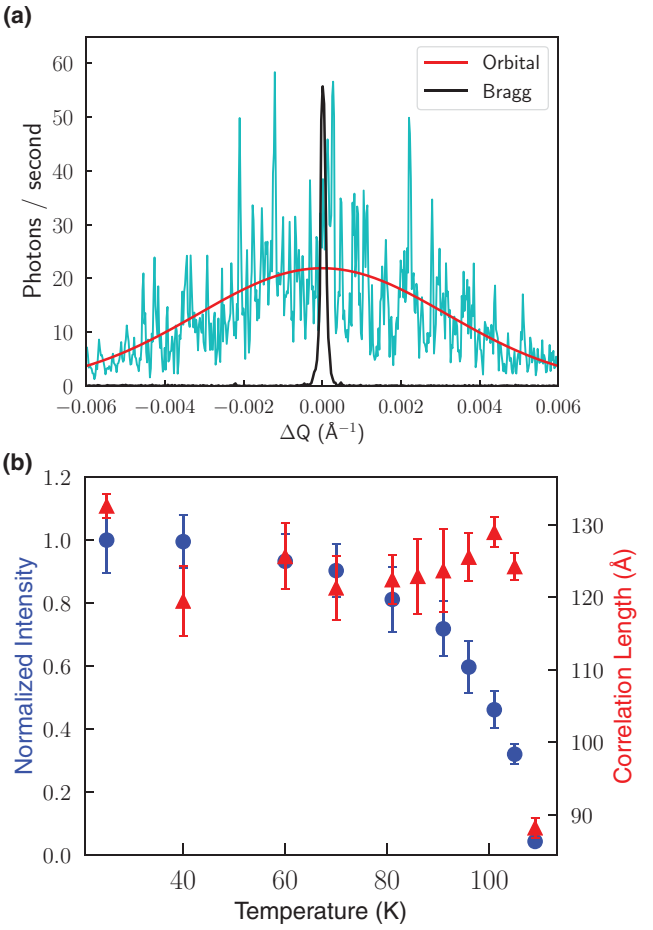

FIG. 3. (a) A line cut through the speckle pattern in Fig. 2 that shows the degree of contrast of the signal. A Gaussian function is fitted to the $(00\frac{1}{2})_c$ orbitally ordered peak, and the (001) lattice reflection is superimposed to show the difference in the orbital and structural correlation lengths. (b) The normalized integrated intensity of the $(00\frac{1}{2})_c$ peak per second at the oxygen K-edge as a function of temperature is plotted along with the correlation length defined by $1/\Delta Q$, where ΔQ is the FWHM of the Gaussian fit to the peak, as seen in (a).

dynamic timescale of the system from how fast or slow the speckle pattern decorrelates in time. This can be quantified by the two-time intensity-intensity autocorrelation function given in Eq. (1), where the intensity of the $(00\frac{1}{2})_c$ peak is correlated pixel-by-pixel with itself at different times, t_1 and t_2, during the entire scan. The normalized correlation plots for the iron L_3-edge and oxygen K-edge at 85 K, 90 K, and 100 K are shown in Fig. 4, but the first 30 to 45 minutes of each scan can be ignored due to instability as the sample equilibrated. The two-time correlation plots for all temperature measurements between 25 K and 109 K can be found in the Supplemental Material [28].

$$g_2(q, t_1, t_2) = \frac{\langle I(q, t_1) I(q, t_2) \rangle}{\langle I(q, t_1) \rangle \langle I(q, t_2) \rangle} \quad (1)$$

From the correlation plots, we see the signal at the iron L_3-edge is continuously dynamic throughout the scan, while

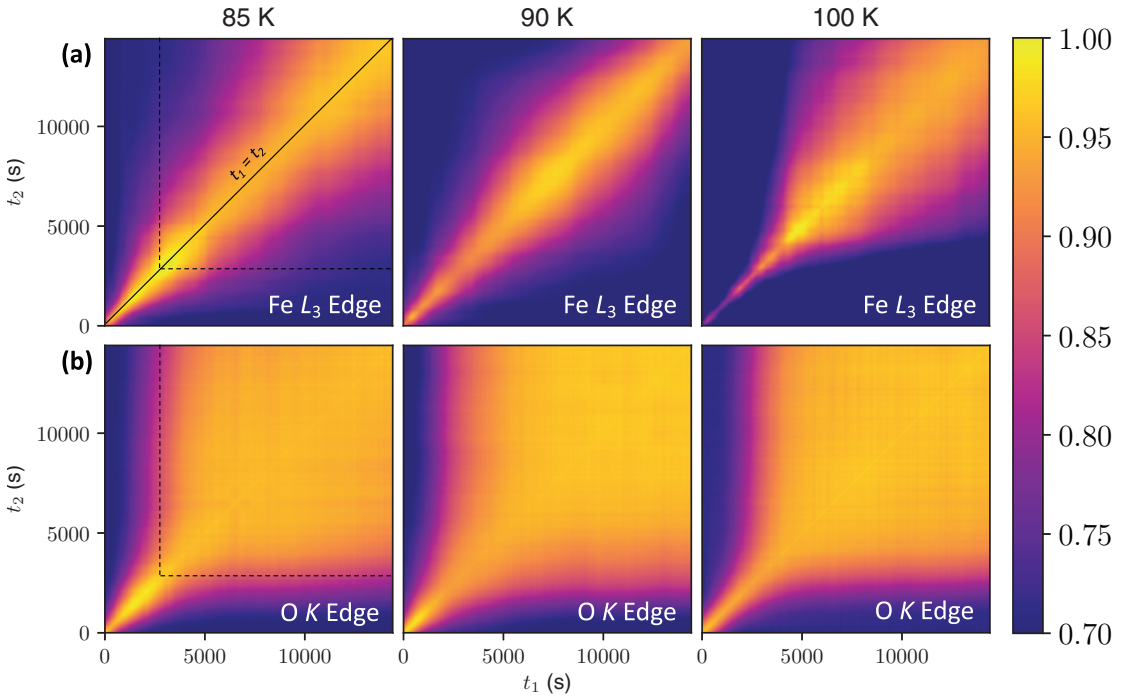

FIG. 4. Normalized two-time intensity-intensity autocorrelation functions defined by Eq. (1) for the (a) iron L_3-edge and the (b) oxygen K-edge at 85 K, 90 K, and 100 K. A 1-s exposure time was used for each scan that lasted 4 hours. The first 30 to 40 minutes of each scan is attributed to sample instability from temperature equilibration; the approximate stable region of the scan is marked by the dashed black line. The $(00\frac{1}{2})_c$ signal at the iron L_3-edge that is sensitive to the iron t_{2g} orbital structure is clearly dynamic whereas the oxygen K-edge signal that is sensitive to the oxygen $2p$ orbital structure remains static.

a static signal is seen at the oxygen K-edge. After normalizing to the average intensity of the speckle pattern, the $t_1 = t_2$ line is the fully correlated reference value, whereas lines orthogonal to $t_1 = t_2$ show increasing delay time between speckle patterns. In Fig. 4, the region where the sample is stable is marked by the dashed black lines, and for the oxygen K-edge signal, the correlation value is approximately the same as the $t_1 = t_2$ value at all points, indicative of a static signal. On the other hand, the correlation value drops away from the $t_1 = t_2$ line for the iron L_3-edge, showing the speckle pattern is changing in time.

We previously showed the dynamics speed up and follow an Arrhenius trend up to 90 K, but slow down until the insulator-to-metal transition temperature at $T = 116$ K [26]. An increasing amount of metallic domains above 90 K spatially reduce the trimeron network, and thus the available hopping sites for the electron. With new results from the oxygen K-edge, we can further conclude that while metallic domains govern the change of characteristic dynamic timescales at the B-site iron t_{2g} states, at a given temperature, the configuration of metallic domains remains static. Both the oxygen K-edge and iron L_3-edge resonant signals are only sensitive to the insulating phase, which can be seen from the drop in total intensity as metallic domains begin to nucleate approaching the metal-insulator transition temperature. If enough thermal energy exists to drive structural fluctuations between metallic and insulating phases at each temperature, that would manifest as a dynamic speckle pattern at both the oxygen K-edge and iron L_3-edge. The static signal at the oxygen K-edge indicates an absence of structural fluctuations between metallic and insulating domains and therefore cannot be the source of the dynamics observed at the iron L_3-edge.

III. DISCUSSION

Ruling out any structural fluctuations, the origin of the dynamic speckle pattern at the iron L_3-edge and the static speckle pattern at the oxygen K-edge must be electronic in nature.

The speckle pattern at the iron L_3-edge is a fingerprint of the orbital-specific electron occupancies—i.e., the unique configuration of Fe^{2+} and Fe^{3+} occupying the t_{2g} orbitals—and any rearrangements to this configuration would alter the speckle pattern. Therefore, the dynamic speckle pattern at the iron L_3-edge indicates a rearrangement of the Fe^{2+} and Fe^{3+} ions within trimeron chains that can only be attributed to thermally driven charge hopping of the conduction electrons. While the charge-hopping mechanism itself is ultrafast and beyond our experimental capabilities, the large activation energy and long timescales observed at the iron L_3-edge indicate that the rate of the charge hopping is infrequent where the overall trimeron network evolves on the order of minutes [26]. Based on well-established theory on orbital ordering in transition-metal oxides and recent studies of the trimeron network [21,26,29], the strength of orbital hybridizations, and consequently the potential for charge dynamics, depends on the degree of orbital overlap between neighboring sites. In the case of magnetite, the interatomic distances of iron cations are shortened within trimeron chains, creating an even stronger orbital overlap that allows for charge dynamics

among the iron cations [12]. Density functional theory and optical magnetic circular dichroism measurements show three dominant pathways for charge dynamics in magnetite [30,31], including direct hopping between neighboring iron-iron sites along the trimeron chains, depicted in Fig. 1(a), and the oxygen-mediated charge transfer via superexchange and double-exchange interactions shown in Fig. 1(b). There is also a ligand-to-metal $p-d$ charge transfer tied to the oxygen $2p$ to Fe^{2+} $3d$ pathway [30] that we can directly detect in our measurements.

The speckle pattern at the oxygen K-edge is a manifestation of the configuration of both the occupied and unoccupied $2p$ orbitals that are also hybridized to the B-site iron t_{2g} orbitals, giving rise to the aforementioned charge transfer pathways. While superexchange and double-exchange interactions will not alter the final state of the oxygen orbital occupations, any direct ligand-to-metal charge dynamics would change the configuration of the oxygen $2p$ orbital network, manifesting as a fluctuating speckle pattern. Our static signal at the oxygen K-edge demonstrates an absence of this pathway in equilibrium, suggesting the charge dynamics in the insulating state of magnetite is due purely to the minority spin electron along the trimeron chains. Finally, the orbital correlation lengths of the B-site iron t_{2g} orbitals (16 nm) and oxygen $2p$ orbitals (13 nm) at $T = 27$ K are on the same order of magnitude. However, this disparity is significant as it corresponds to a FWHM difference of approximately ~ 100 pixels in our experimental conditions, well beyond the error of margin. Even though the intricately linked iron t_{2g} and oxygen $2p$ orbitals give rise to the resonant $(00\frac{1}{2})_c$ peak, the difference in orbital correlation lengths suggests there is still an unknown mechanism that leads to this spatial decoupling. This is also supported by the anomalous uptick of the correlation length near the transition temperature seen in Fig. 3(b) and a similar anomalous uptick in the peak intensity in seen in [22], both of which are seen at the oxygen K-edge but not at the iron L_3−edge.

IV. CONCLUSION

We have shown an experimental approach that uses XPCS at resonant elastic geometry to probe the site- and element-specific charge-orbital dynamics in magnetite directly by exploiting a Bragg-forbidden orbitally ordered peak. Our results, contrary to Verwey's hypothesis that the conduction electron freezes in the insulating state, show there is still sufficient thermal energy in the system to drive these electrons to hop along trimeron chains. The extremely stable configuration of the oxygen $2p$ orbital network further suggests that only the minority spin electron of the iron cations within trimeron chains play a role in the Verwey transition [32,33]. Finally, magnetite belongs to a class of transition-metal oxides where the interaction of the transition-metal $3d$ electrons with the field of O^{2-} ligands is responsible for many fascinating nanoscale effects that give rise to various classes of electronically ordered materials [14,24,29,34]. In this study, we specifically tuned to the oxygen K-edge resonant energy and the iron L_3−edge resonant energy corresponding to the oxygen $2p$ and octahedral t_{2g} orbitals, respectively, but further XPCS measurements with varying polarizations at specific points in the iron $L_{2,3}$-edge spectrum can reveal distinct dynamic timescales from the e_g orbitals or A-site iron $3d$ states. With new-generation coherent x-ray sources, we can employ the same experimental technique to reveal unseen dynamical trends in other materials with strong electron correlations, such as nickelates and cuprates. For example, the charge-order structure of high-temperature cuprate superconductors has long been attributed to the strong hybridization between the copper $3d$ and oxygen $2p$ orbitals, but recent studies revealed spatially localized charge excitations associated with oxygen sites in $La_{2-x}Ce_xCuO_4$ that seem to defy the strong hybridization between copper and oxygen [35]. In $La_{1.875}Ba_{0.125}CuO_4$ cuprates, resonant XPCS measurements revealed a stable charge density wave order detected at the copper L_3−edge, but this study lacked measurements at the oxygen K-edge [36,37]. Our XPCS study demonstrates an effective method that exploits the transition metal L-edges in tandem with the oxygen K-edge to pinpoint the origin of emergent behaviors.

ACKNOWLEDGMENTS

The fabrication of samples at UCSD was supported by AFOSR Grant No. FA9550-16-1-0026 and NSF Award No. DMR-1411335. The coherent x-ray scattering experiment was supported by U.S. Department of Energy, Office of Science, Office of Basic Energy Sciences, under Contract No. DE–SC0001805 (coherent x-ray scattering, N.H. and O.G.S.) J.L. and R.K. were supported by a grant from the National Science Foundation (DMR-1902652). This research used resources from the 23-ID-1 Coherent Soft X-Ray Scattering (CSX) beamline of the National Synchrotron Light Source II, a U.S. Department of Energy (DOE) Office of Science User Facility operated for the DOE Office of Science by Brookhaven National Laboratory under Contract No. DE-SC0012704.

[1] M. Imada, A. Fujimori, and Y. Tokura, Rev. Mod. Phys. **70**, 1039 (1998).
[2] E. Dagotto, Science **309**, 257 (2005).
[3] Y. Yanase, T. Jujo, T. Nomura, H. Ikeda, T. Hotta, and K. Yamada, Phys. Rep. **387**, 1 (2003).
[4] M. A. Hossain, I. Zegkinoglou, Y.-D. Chuang, J. Geck, B. Bohnenbuck, A. G. Cruz Gonzalez, H.-H. Wu, C. Schüßler-Langeheine, D. G. Hawthorn, J. D. Denlinger, R. Mathieu, Y. Tokura, S. Satow, H. Takagi, Y. Yoshida, Z. Hussain, B. Keimer, G. A. Sawatzky, and A. Damascelli, Sci. Rep. **3**, 2299 (2013).
[5] J. J. Turner, K. J. Thomas, J. P. Hill, M. A. Pfelfer, K. Chesnel, Y. Tomioka, Y. Tokura, and S. D. Kevan, New J. Phys. **10**, 053023 (2008).
[6] Y. D. Chuang *et al.*, Phys. Rev. Lett. **110**, 127404 (2013).
[7] S. L. Zhang, A. Bauer, H. Berger, C. Pfleiderer, G. van der Laan, and T. Hesjedal, Phys. Rev. B **93**, 214420 (2016).
[8] E. J. Verwey, P. W. Haayman, and F. C. Romeijn, J. Chem. Phys. **15**, 181 (1947).
[9] M. Coey, Nature (London) **430**, 155 (2004).

[10] M. Iizumi, T. F. Koetzle, G. Shirane, S. Chikazumi, M. Matsui, and S. Todo, Acta Cryst. B **38**, 2121 (1982).
[11] E. J. W. Verwey, Nature (London) **144**, 327 (1939).
[12] M. S. Senn, J. P. Wright, and J. P. Attfield, Nature (London) **481**, 173 (2011).
[13] J. P. Wright, J. P. Attfield, and P. G. Radaelli, Phys. Rev. B **66**, 214422 (2002).
[14] D. I. Khomskii and M. V. Mostovoy, J. Phys. A: Math. Gen. **36**, 9197 (2003).
[15] K. I. Kugel and D. I. Khomskii, Zh. Eksp. Teor. Fiz. **64**, 1429 (1973) [Sov. Phys. JETP **37**, 725 (1973)].
[16] K. I. Kugel and D. I. Khomskii, Sov. Phys. Usp. **25**, 231 (1982).
[17] G. Subías, V. Cuartero, J. García, J. Herrero-Martin, J. Blasco, M. C. Snchez, and F. Yakhou, J. Phys.: Conf. Ser. **190**, 012085 (2009).
[18] J. Schlappa, C. Schüßler-Langeheine, C. F. Chang, H. Ott, A. Tanaka, Z. Hu, M. W. Haverkort, E. Schierle, E. Weschke, G. Kaindl, and L. H. Tjeng, Phys. Rev. Lett. **100**, 026406 (2008).
[19] D. J. Huang, H. J. Lin, J. Okamoto, K. S. Chao, H. T. Jeng, G. Y. Guo, C. H. Hsu, C. M. Huang, D. C. Ling, W. B. Wu, C. S. Yang, and C. T. Chen, Phys. Rev. Lett. **96**, 096401 (2006).
[20] J. García and G. Subías, J. Phys.: Condens. Matter **16**, R145 (2004).
[21] M. Hepting, *Introduction: Transition Metal Oxides and Their Heterostructures* (Springer, Cham, Switzerland, 2017).
[22] S. B. Wilkins, S. Di Matteo, T. A. W. Beale, Y. Joly, C. Mazzoli, P. D. Hatton, P. Bencok, F. Yakhou, and V. A. M. Brabers, Phys. Rev. B **79**, 201102(R) (2009).
[23] I. Leonov, A. N. Yaresko, V. N. Antonov, M. A. Korotin, and V. I. Anisimov, Phys. Rev. Lett. **93**, 146404 (2004).
[24] J. Suntivich, W. T. Hong, Y. L. Lee, J. M. Rondinelli, W. Yang, J. B. Goodenough, B. Dabrowski, J. W. Freeland, and Y. Shao-Horn, J. Phys. Chem. C **118**, 1856 (2014).
[25] H. Elnaggar, R. Wang, M. Ghiasi, M. Yañez, M. U. Delgado-Jaime, M. H. Hamed, A. Juhin, S. S. Dhesi, and F. De Groot, Phys. Rev. Mater. **4**, 024415 (2020).
[26] R. Kukreja, N. Hua, J. Ruby, A. Barbour, W. Hu, C. Mazzoli, S. Wilkins, E. E. Fullerton, and O. G. Shpyrko, Phys. Rev. Lett. **121**, 177601 (2018).
[27] W. Eerenstein, T. T. M. Palstra, T. Hibma, and S. Celotto, Phys. Rev. B **66**, 201101(R) (2002).
[28] See Supplemental Material at https://link.aps.org/supplemental/10.1103/PhysRevMaterials.7.014413 for thin-film fabrication details, structural characterizations, and normalized two-time correlations for all temperatures.
[29] Y. Tokura and N. Nagaosa, Science **288**, 462 (2000).
[30] J. Chen, H.-S. Hsu, Y.-H. Huang, and D.-J. Huang, Phys. Rev. B **98**, 085141 (2018).
[31] W. F. J. Fontijn, P. J. Van der Zaag, M. A. C. Devillers, V. A. M. Brabers, and R. Metselaar, Phys. Rev. B **56**, 5432 (1997).
[32] G. Perversi, E. Pachoud, J. Cumby, J. M. Hudspeth, J. P. Wright, S. A. J. Kimber, and J. Paul Attfield, Nat. Commun. **10**, 2857 (2019).
[33] A. Bosak, D. Chernyshov, M. Hoesch, P. Piekarz, M. Le Tacon, M. Krisch, A. Kozlowski, A. M. Oles, and K. Parlinski, Phys. Rev. X **4**, 011040 (2014).
[34] J. P. Hill, C. S. Nelson, M. V. Zimmermann, Y. J. Kim, D. Gibbs, D. Casa, B. Keimer, Y. Murakami, C. Venkataraman, T. Gog, Y. Tomioka, Y. Tokura, V. Kiryukhin, T. Y. Koo, and S. W. Cheong, Appl. Phys. A Mater. Sci. Process. **73**, 723 (2001).
[35] A. Nag, M. Zhu, M. Bejas, J. Li, H. C. Robarts, H. Yamase, A. N. Petsch, D. Song, H. Eisaki, A. C. Walters, M. García-Fernández, A. Greco, S. M. Hayden, and K.-J. Zhou, Phys. Rev. Lett. **125**, 257002 (2020).
[36] X. M. Chen, V. Thampy, C. Mazzoli, A. M. Barbour, H. Miao, G. D. Gu, Y. Cao, J. M. Tranquada, M. P. M. Dean, and S. B. Wilkins, Phys. Rev. Lett. **117**, 167001 (2016).
[37] V. Thampy, X. M. Chen, Y. Cao, C. Mazzoli, A. M. Barbour, W. Hu, H. Miao, G. Fabbris, R. D. Zhong, G. D. Gu, J. M. Tranquada, I. K. Robinson, S. B. Wilkins, and M. P. M. Dean, Phys. Rev. B **95**, 241111(R) (2017).